Investigation of Bulk Carrier Open-Water Performance Using CFD Methods

F. Jahra* and D. C. Seo*
Corresponding author: fatima.jahra@nrc-cnrc.gc.ca
* Ocean, Coastal and River Engineering, National Research Council Canada.

Abstract: This study presents a comprehensive, step-by-step investigation into the calm-water performance of a bulk carrier using Computational Fluid Dynamics (CFD) analysis. The SOBC-1 hull form (SINTEF Ocean Bulk Carrier No. 1) was selected as the reference model. This research examines propeller open-water performance, ship hull resistance and self-propulsion characteristics. Numerical simulation results of the propeller's open-water characteristics were compared with physical model test data. Resistance tests were conducted at the design waterline (DWL) using the appended hull form, allowing for free trim and sinkage. Propulsion tests were then carried out at a specified speed, capturing the propeller-hull interaction through a sliding mesh technique with an actual rotating propeller. Additionally, a body-force propeller method (also known as virtual disk model) was applied to repeat the self-propulsion simulation under the same operating condition. The performance of the two self-propulsion prediction approaches were compared in terms of computational cost, mesh requirements, and accuracy relative to model test data. Based on these comparisons, recommendations are provided for made regarding the more computationally efficient methodology. A three-dimensional wake study was also conducted at DWL and at the same speed as the SPP analysis. The CFD predictions showed good agreement with all corresponding model test results. Considering the uncertainties in both the CFD models and the physical model test, the predicted outcomes were found to aligned well within the uncertainty limits.

Keywords: Computational Fluid Dynamics (CFD), Bulk carrier, Propeller open-water characteristics, Resistance and propulsion analysis, Body force propeller method, Wake study.

1. Introduction

With advances in modelling techniques and computational resources, Computational Fluid Dynamics (CFD) has become an essential tool in marine hydrodynamics, supporting both engineering applications and fundamental research. CFD is now widely applied in ship hydrodynamic performance assessment throughout the design cycle, from the concept and preliminary design stages to detailed design and retrofit studies, owing to its cost- and time-effectiveness compared with conventional towing-tank experiments and full-scale sea trials. A key advantage of CFD is its capability to perform simulations directly at full scale, thereby reducing uncertainties associated with Reynolds number effects, commonly referred to as scale effects, which are inherent in model-scale testing ([1]).

Despite these advantages, CFD predictions are subject to modelling and numerical uncertainties and therefore must be verified and validated against experimental data obtained from physical model tests or full-scale measurements to ensure their accuracy and reliability. Once an adequate level of verification and validation has been achieved, CFD can be confidently applied to investigate a wide range of operating conditions and design scenarios that would otherwise be difficult, time-consuming, or prohibitively expensive to examine experimentally. Consequently, consistent with ITTC recommendations, rigorous verification and validation (V&V) of CFD methods constitute a prerequisite for their reliable application in ship hydrodynamic performance prediction.

Over the past few years, numerous researchers have conducted numerical investigations using CFD methods to evaluate the open-water performance of propellers of various types ([2], [3], [4], [5]), as well as the hydrodynamic performance of appended and bare hulls ([1], [4], [6], [7], [8], [9]). In addition, CFD has been widely applied to investigate ship maneuvering and seakeeping characteristics under a broad range of environmental conditions ([10], [11], [12]).

In the public domain, experimental data on ship resistance and propulsion available for verification, validation, and calibration (V&V) purposes are largely limited to model-scale test results, with benchmark ship cases such as the KCS, KVLCC1, KVLCC2, JBC, DTMB 5415, DTC, MV REGAL etc. With only a few exceptions, most studies have therefore focused on model-scale CFD simulations, validating numerical predictions against corresponding physical model test data. Krasilnikov et al. ([1]) conducted a CFD analysis using a blind simulation exercise at ship scale, applying the commercial software STAR-CCM+ to the MV REGAL vessel, one of the benchmark ships studied within the Joint Industry Project JoRes ([13]). Their study investigated propeller open-water characteristics, ship towing resistance, and self-propulsion performance, and directly compared CFD predictions with full-scale performance estimates derived from model tests conducted at SINTEF Ocean and sea trial data obtained within the JoRes project. Yu et al. ([4]) performed verification and validation of the total resistance of the KRISO Container Ship (KCS) in calm water and evaluated mesh and time-step uncertainties using the CFD solver naoe-FOAM-SJTU, concluding that time-step uncertainty was insignificant for the investigated conditions. Wilson et al. ([6]) applied an unsteady Reynolds-Averaged Navier–Stokes (URANS) solver (CFDSHIP-IOWA) to investigate wave-breaking characteristics of the R/V Athena I at three different speeds. They reported that at a high Froude number (Fr = 0.62), intense bow wave breaking occurred, characterized by repeated reconnection of plunging breakers with the free surface and the generation of multiple free-surface scars. Jahra et al. ([7]) conducted model-scale CFD simulations applying STAR-CCM + to investigate hydrodynamic loads and flow patterns acting on an escort tug under various oblique flow conditions, demonstrating good agreement between numerical predictions and experimental data. Islam et al. ([8]) reported the hydrodynamic performance of an FPSO subjected to highly oblique flow conditions and validated their CFD model through comparison with physical model test results. Ahmed et al. ([9]) employed the commercial software ANSYS CFX to compute total resistance and the flow field around Wigley and DTMB 5415 hull forms at model scale, reporting prediction errors of less than 6% relative to experimental measurements. Aram and Mucha ([10]) simulated turning-circle and zig-zag maneuvers of the Office of Naval Research Tumblehome (ONRTH) vessel using STAR-CCM+, applying different propeller modeling approaches to assess maneuvering performance against model test data. Their results showed that a discretized propeller model provided more accurate maneuvering predictions than a body-force propeller (BFP) model. Deng et al. ([11]) conducted zig-zag and turning-circle maneuver simulations in calm water for the ONRT and KCS hull forms using the ISIS-CFD solver, comparing predicted ship motions with experimental measurements to evaluate numerical accuracy for different propeller representations, including actual propeller, body-force propeller, and frozen-rotor-type methods. Zou et al. ([12]) evaluated numerical errors and uncertainties for an unappended tanker performing maneuvering motions at different drift angles and water depths and validated their simulations through comparison with experimental data.

The present study presents a step-by-step CFD-based procedure for predicting the calm-water hydrodynamic performance of a bulk carrier. The SINTEF Ocean Bulk Carrier (SOBC-1) is selected as the reference hull form. Model test results reported by SINTEF Ocean AS ([14]) are reproduced using high-fidelity CFD simulations. The referenced report includes propeller open-water performance, ship resistance, and self-propulsion analyses. Most previous benchmark cases have primarily focused on resistance prediction. The SOBC-1 case provides comprehensive data, making it a convenient reference for consistently exploring a typical hull performance evaluation process. The aim of this study was to predict the full-scale performance of the vessel using CFD and to compare the prediction results with those obtained through the traditional model test approach. The ship scale study aims to eliminate the Reynolds scaling effect. Furthermore, the study seeks to identify the most critical step(s) within the evaluation process that may contribute to significant prediction errors.

Numerical predictions of propeller open-water characteristics are compared with physical model test data. Resistance simulations are conducted at the design waterline (DWL) for the appended hull form under free sinkage and trim conditions. Subsequently, propulsion simulations are performed at the specified operating speed, and the self-propulsion point (SPP) is identified using a sliding-mesh approach with an actual rotating propeller. Then, the actual propeller was replaced with a body force propeller method (also known as virtual disk method), and the same self-propulsion analysis was repeated. The performance of the two SPP estimations were compared in terms of computational cost, mesh requirements, and accuracy relative to model test data with recommendations made for the more efficient method. A three-dimensional wake study was also conducted at DWL and at the same speed as the SPP analysis.

Except for the propeller open-water performance analysis and wake survey, all simulations were conducted at full (ship) scale. Furthermore, a detailed grid-sensitivity study for hull resistance and propeller open water analysis was conducted to establish confidence in the numerical approach and its applicability to a wide range of ship hull forms.

2. Overview of the Geometry

The geometry of the design propeller and the SOBC-1 hull was provided by SINTEF Ocean ([14], [15]). Calm-water performance model tests were conducted using the controllable pitch propeller (CPP), including the hub using a 1:32.0 scaled model. The propeller open-water performance was simulated at the same model scale using a CFD approach, whereas the resistance and self-propulsion analyses were performed at ship scale. Figure 1 and Figure 2 illustrate the propeller and hull geometries employed in the CFD simulations and the physical model tests, respectively. For the resistance prediction analyses, hull model was equipped with a rudder only. Main particulars of the hull and propeller is shown in Table 1. All parameters are presented in ship scale.

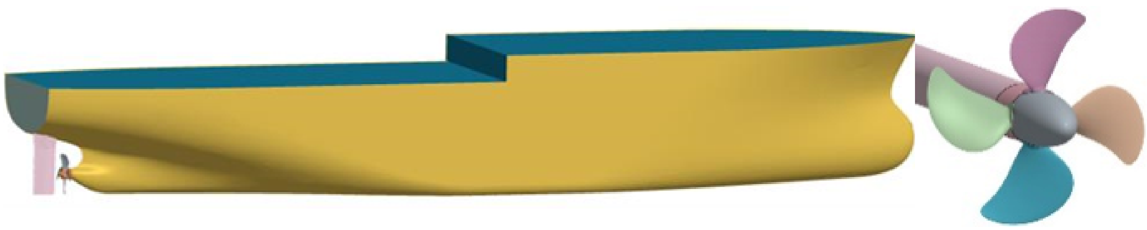

Figure 1: SOCB-1 hull and the CP propeller geometry for CFD analysis.

Figure 2: SOCB-1 hull and the CP propeller geometry for physical model tests ([16].

Table 1: Main Particulars of SOBC-1 Hull and CP Propeller

Main Particulars	
Length between perpendiculars, L_{PP}	190 m
Length on waterline, L_{WL}	196.942 m
Breadth waterline, B_{WL}	32.2 m
Draught at $L_{PP}/2$	11.0 m
Volume displacement, ∇	48956.71 m^3
Wetted surface area, S	8576.74 m^2
Propeller type (Model no. P1608)	CPP
Propeller diameter, D	6.75 m
Hub diameter ratio, d/D	0.252

3. Description of Numerical Analysis Methods

3.1 Numerical Approach

In this study, the commercial CFD code STAR-CCM+ (version 2506) was employed. An unsteady Reynolds-Averaged Navier-Stokes (URANS) solver was used in conjunction with the SST k-ω turbulence model. For both resistance and propulsion simulations, the free-surface effects were resolved using the Volume of Fluid (VOF) method with a modified High-Resolution Interface Capturing (MHRIC) scheme implemented in STAR-CCM+. Pressure-velocity coupling was achieved using the Semi-Implicit Method for Pressure-Linked Equations (SIMPLE) algorithm. Calm-water resistance and self-propulsion simulations were performed using the Dynamic Fluid-Body Interaction (DFBI) module, allowing free heave and pitch motions under hydrodynamic loading at the test speed. The simulations were conducted in accordance with ITTC-recommended procedures for propeller open-water, resistance, and self-propulsion analyses. The propeller open-water performance predictions were carried out using a rigid-body motion (sliding-mesh) approach, consistent with ITTC best practices, to accurately quantify propeller thrust and torque.

The governing equations for the incompressible viscous fluid, along with the two-equation k-ω SST turbulence model, are provided below. Details of the notations and symbols used in the equations are available in [17].

$$\frac{\partial \bar{u}_i}{\partial x_i} = 0 \tag{1}$$

$$\frac{\partial(\rho \bar{u}_i)}{\partial t} + \frac{\partial}{\partial x_j}\left(\rho \bar{u}_i \bar{u}_j + \rho \overline{u'_i u'_j}\right) = -\frac{\partial \bar{p}}{\partial x_i} + \frac{\partial \bar{\tau}_{ij}}{\partial x_j} \tag{2}$$

$$\frac{\partial \rho k}{\partial t} + \frac{\partial}{\partial x_j}\left[\rho u_j k - (\mu + \sigma_k \mu_t)\right] = \tau_{ij} S_{ij} - \beta^* \rho \omega k \tag{3}$$

$$\frac{\partial \rho \omega}{\partial t} + \frac{\partial}{\partial x_j}\left[\rho u_j \omega - (\mu + \sigma_\omega \mu_t)\frac{\partial \omega}{\partial x_j}\right] = P_\omega - \beta \rho \omega^2 + 2(1 - F_1)\frac{\rho \sigma_\omega}{\omega}\frac{\partial k}{\partial x_j}\frac{\partial \omega}{\partial x_j} \tag{4}$$

The time-step size was selected according to the type of analysis, including propeller open-water performance prediction, calm-water resistance simulations, and self-propulsion analyses using either an actual rotating propeller or a body-force propeller method. For the propeller open-water simulations and the self-propulsion point (SPP) analysis with an actual rotating propeller, the time-step size corresponded to 4° of propeller rotation per time step. When employing the body-force propeller method, the time-step size was determined according to the ship's convective time scale, set to 0.2% of L_{pp}/V_s. Here, V_s represents the velocity of the vessel.

All simulations were conducted using water properties specified in the case description provided by SINTEF Ocean ([14]). A water temperature of 16°C was applied for the propeller open-water performance analysis, while a temperature of 15°C, along with the corresponding water density, was used for the ship-scale resistance and propulsion analyses.

3.2 Computational Domain

Propeller open-water performance prediction analysis was performed in model scale (1:32.0). The computational domain, including the refinement zones and mesh distribution used for the propeller open-water performance prediction, is shown in Figure 3. The domain extends approximately $7.5D$ downstream and $2.5D$ upstream from the propeller center. Local mesh refinement was applied in the vicinity of the propeller blades, with refinement tubes positioned around the blade tips to accurately resolve pressure gradients and capture the flow features along the blade edges. A polyhedral mesh was employed throughout the computational domain. Boundary conditions applied for the simulation is also shown in the figure.

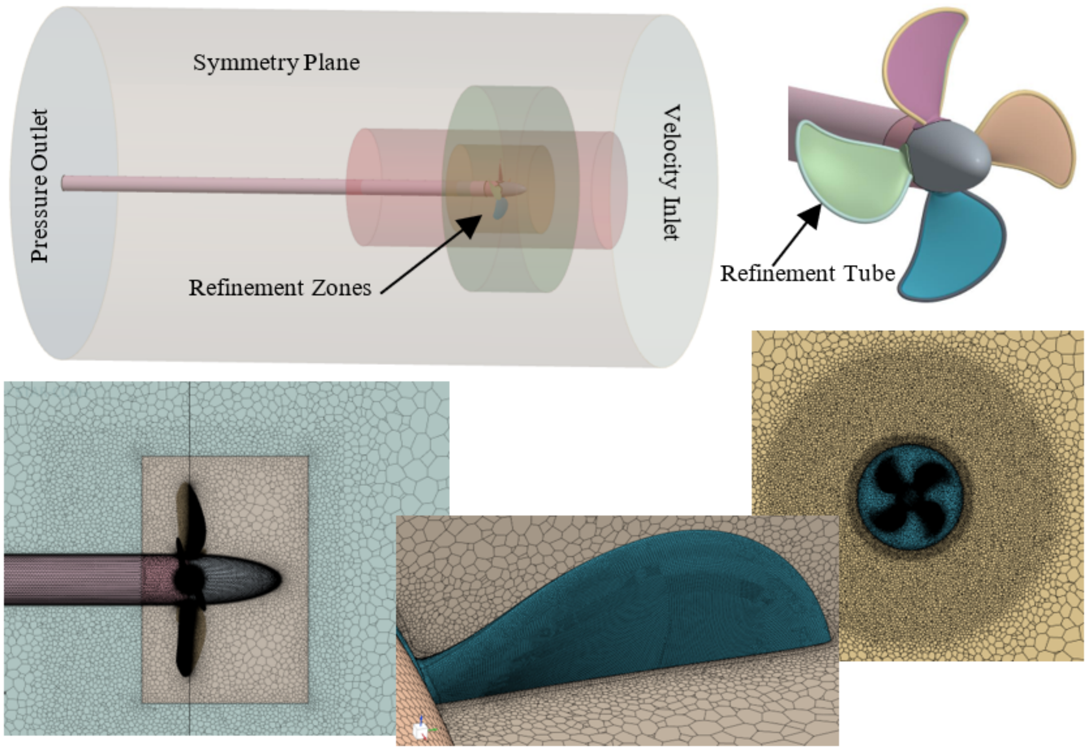

Figure 3: Computational domain and mesh distribution for propeller open-water simulations.

For calm-water resistance prediction, CFD simulations were performed at ship scale using a half-body model to reduce computational cost. In contrast, full-body simulations were conducted for the SPP analysis, including an explicitly modeled rotating propeller. The computational domain, refinement zones, boundary conditions, and mesh distribution are shown in Figure 4. For the half-body simulations, a symmetry plane boundary condition was applied along the ship centerline. The domain extends approximately $3.0L_{pp}$ downstream and $3.0L_{pp}$ upstream from the aft of the vessel, with the side boundaries located approximately $2.0L_{pp}$ from the ship centerline. Local mesh refinement blocks were applied near the bow, stern, rudder, and stern-wave region. Additional refinement was applied to capture the Kelvin wake pattern, including the characteristic wave wedge, ensuring accurate resolution of wave-making effects.

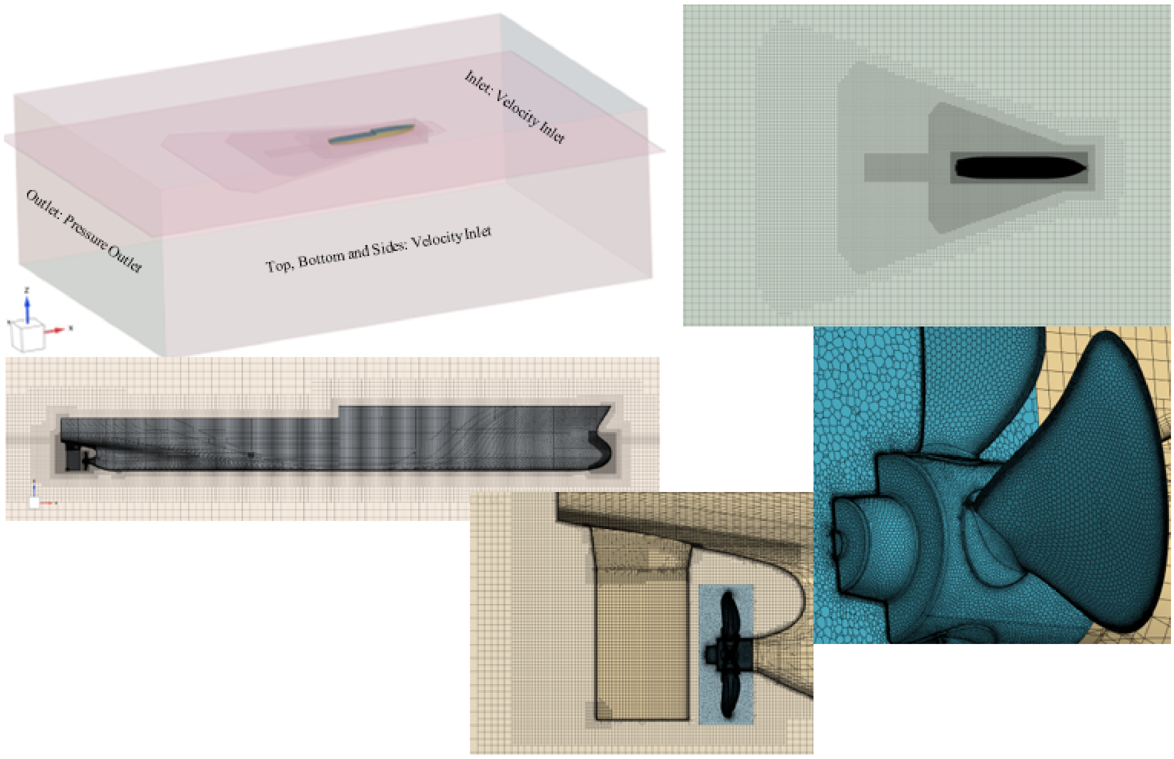

Figure 4: Computational domain and mesh distribution for SPP analysis.

3.3 Uncertainty Assessment

Uncertainty analysis is an integral part of CFD analysis and is as important as it is for physical model testing. Conducting uncertainty analysis is essential for assessing the accuracy of CFD predictions ([18]). Sensitivity studies, along with the consequent uncertainty and risk analyses, can be performed not only for input data and parameters but also for differing conceptual models, often referred to as structural uncertainty or model-form uncertainty. Sensitivity analysis is an important part of validation comparisons, providing deeper understanding for both computational analysts and experimentalists ([19]).

A mesh sensitivity analysis was performed for both the propeller open-water performance simulation, and the resistance and propulsion (R&P) analysis, following the method proposed by Stern et al. ([20]), as outlined in the ITTC (2024) recommended procedure for verification studies. A uniform grid refinement ratio of r= $\sqrt{2}$ was adopted between successive mesh levels.

A grid convergence study for the resistance simulation was performed using base sizes of 1.75 m, 2.5 m, and 3.5 m. The resulting convergence ratio, $R = 0.55$, satisfies the monotonic convergence criterion (0 < R < 1) (ITTC, 2024), indicating consistent grid convergence. Table 2 summarizes the mesh sensitivity analysis for the resistance simulations.

An uncertainty analysis was subsequently conducted to select the appropriate base mesh size for the resistance and self-propulsion point (SPP) analyses. Under the monotonic convergence condition, the generalized Richardson Extrapolation (RE) method was applied to estimate the numerical uncertainty. Using solutions from three successive grid levels, the leading-order error term was evaluated, allowing estimation of the observed order of accuracy (p_{RE}) and the discretization error (δ_{RE}). Xing and Stern (2010) ([21] defined the distance metric P as the ratio of the estimated order of accuracy (p_{RE}) to the theoretical order of accuracy ($p_{th} = 2$) (ITTC, 2024). The distance metric P is used to calculate the factor of safety. A factor of safety (FS) approach proposed by Roache (1998) ([19]) was used to define the numerical uncertainty U_{FS}. Table 3 summarizes the uncertainty assessment results. The equations for the estimation are as follows:

$$p_{RE} = \frac{\ln(\varepsilon_{32}/\varepsilon_{21})}{\ln(r)} \tag{5}$$

$$\delta_{RE} = \frac{\varepsilon_{21}}{r^p - 1} \tag{6}$$

$$P = p_{RE}/p_{th} \tag{7}$$

$$FS(P) = \begin{cases} 2.45 - 0.85P, & 0 < P \le 1 \\ 16.4P - 14.8, & P > 1 \end{cases} \tag{8}$$

$$U_{FS} = FS \cdot |\delta_{RE}| \tag{9}$$

The spatial verification study established monotonic convergence, with an estimated numerical order of accuracy ($p_{RE} = 1.71$) matching well with the theoretical second-order limit. Adhering to the ITTC guidelines, the absolute grid uncertainty was calculated as $U_{FS} = 4.05$ kN, which represents a relative discretization error of 0.716% on the finest mesh (S_1). The medium grid (S_2) yielded a remarkably similar uncertainty of 0.714%. This minor variance of 0.0024% confirms that the numerical framework operates securely within the asymptotic convergence range. These numerical uncertainty metrics indicate that the discretization errors are small, confirming that the numerical predictions are sufficiently grid-independent and reliable for the present analysis. To optimize computational efficiency, the medium grid topology (3.90M cells, 2.5 m base size) was selected as the core configuration for the primary hull resistance curves. Conversely, the refined 1.75 m base mesh (S_1, 8.15M cells) was deployed for the transient self-propulsion point (SPP) simulations to rigorously capture localized propeller-hull wake interaction dynamics.

For the propeller open-water simulations, a mesh sensitivity analysis was conducted using three base cell sizes: 0.10 m, 0.075 m, and 0.05 m, corresponding to approximately 2.6, 2.9, and 3.51 million volume elements, respectively. No significant differences were observed in the predicted thrust and torque coefficients across the three mesh configurations. However, the propeller-induced vortex structures were more distinctly visible with the finer mesh arrangements. Based on a balance between numerical accuracy and computational cost, a base cell size of 0.075 m was adopted for predicting the open-water performance curves in the present analysis.

Table 2: Details of Mesh Sensitivity Analysis.

Grid Density	**Base Grid Size [m]**	**Number of Volume Elements for Half-Hull**	**Total Resistance [kN]**
Fine, S_1	1.75	8.15×10^6	565.91
Medium, S_2	2.5	3.90×10^6	567.81
Coarse, S_3	3.5	2.61×10^6	571.23

The mesh configurations adopted for the propeller open-water and R&P analyses, corresponding to the applied base cell sizes, are illustrated in Figure 3 and Figure 4, respectively.

In the present study, an uncertainty analysis was conducted for three types of free-surface capturing schemes. Calm-water resistance simulations were performed at a vessel speed of 15 knots using the 1st-order scheme, the High-Resolution Interface Capturing (HRIC) scheme, and the MHRIC scheme. A comparison was made between the predicted resistance, dynamic sinkage, and trim values and the corresponding experimental fluid dynamics (EFD) data.

Table 3: Uncertainty assessment results following the ITTC recommended verification procedure.

Test item	
Convergence Analysis	
Refinement ratio, r	1.414
Resistance changes between medium and fine ($\varepsilon_{21} = S_2 - S_1$)	1.895
Resistance changes between coarse and medium ($\varepsilon_{32} = S_3 - S_2$)	3.423
Convergence ratio, $R = \varepsilon_{21}/\varepsilon_{32}$	0.554
Uncertainty Analysis	
Theoretical order of accuracy, p_{th}	2.000
Estimated order of accuracy, p_{RE}	1.706
Estimated error, δ_{RE}	2.350
Distance metric, P	0.853
Factor of safety, FS	1.725
Uncertainty, U_{FS}	4.054
$U_{FS}(\%S_1)$	0.716
$U_{FS}(\%S_2)$	0.714

The results showed that the HRIC scheme produced the lowest percentage errors compared to the other two schemes; however, it also required the highest solver elapsed time. The MHRIC scheme is recommended for calm-water resistance or self-propulsion prediction (SPP) cases where excessive resolution of small droplets or bubbles is not required. The 1st-order scheme resulted in the lowest solver elapsed time and is therefore only suitable for the early design stage of a hull, where fast computation is prioritized over the accurate prediction of hydrodynamic parameters. Thus, in the present study, all resistance and SPP analyses were conducted using the MHRIC scheme.

Figure 5 shows the flow fields captured by the three different schemes. It can be observed that there is no significant difference between the flow fields or free-surface elevation profiles predicted by the HRIC and MHRIC schemes. Table 4 presents the comparison between the EFD and CFD results obtained using the three schemes. In the table, the percentage of Error is calculated as

$$\frac{EFD - CFD}{EFD} \times 100$$

Table 4: Comparison Between the EFD Results and CFD Predictions Using Three Free-Surface Capturing Schemes.

Convection Scheme	**Solver Elapsed Time per Time Step [s]**	**Trim [deg]**	**Sinkage [m]**	**Sinkage AP [m]**	**Sinkage FP [m]**	$C_T \times 10^3$	**Trim Error [%]**	**Sinkage Error [%]**	C_T **Error [%]**
1st-order	9.5	0.175	-0.243	0.060	-0.521	2.573	-4.79	3.57	-21.75
HRIC	20.2	0.171	-0.246	0.051	-0.517	2.140	-2.40	2.38	-1.27
MHRIC	12.4	0.168	-0.245	0.047	-0.512	2.162	-0.60	2.78	-2.32
EFD	–	0.167	-0.252	0.025	-0.529	2.113	–	–	–

All simulations were executed on an HPC system utilizing 42 processors (AMD EPYC 7742, 64 cores, 2.25 GHz, 503 GB RAM).

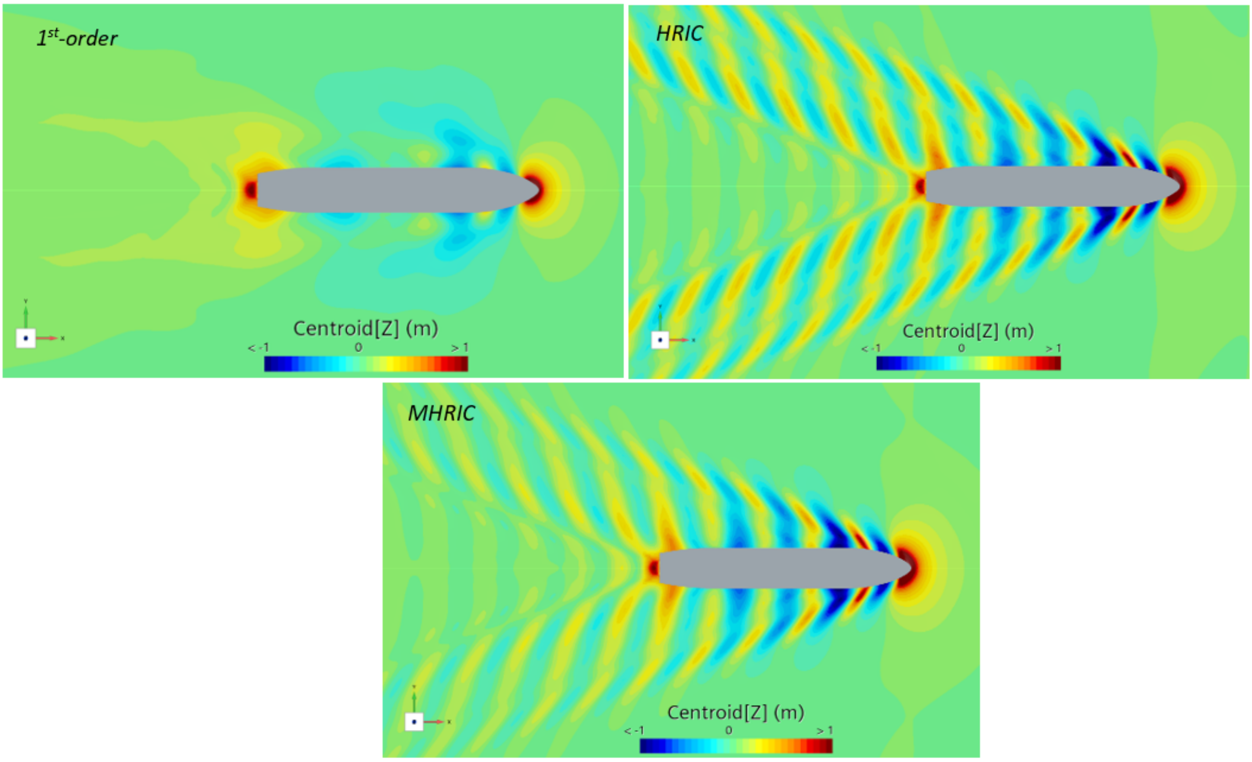

Figure 5: Free-Surface Elevation for Three Free-Surface Capturing Schemes.

4. Results and Discussions

4.1 Propeller Open-water Performance Analysis

The propeller open-water performance analysis was carried out for the P1608 propeller model. All simulations were performed at model scale (1:32.0). The propeller geometry used in the CFD analysis was also provided by SINTEF Ocean. The propeller is a four-bladed controllable-pitch (CP) propeller with a pitch ratio of 0.97 at r/R=0.7.

To ensure consistency with experimental conditions, only modification made to the provided CAD model was the addition of the shaft and hub cone, which were not included in the original geometry, as illustrated in Figure 3.

The open-water simulations were conducted under the same conditions as the physical model tests, with a propeller rotational speed of 14 revolutions per second (RPS) and water properties corresponding to a temperature of 16°C. The applied computational grid in the propeller open-water simulation is shown in Figure 3. A rigid-body motion (sliding-mesh) approach was employed to represent the rotating propeller geometry.

A wall-function approach was applied in the near-wall region, and the mesh was designed to maintain an average wall y^+ value of approximately 30, particularly around the propeller blade surfaces, as illustrated in Figure 6. The propeller open-water performance curves, including thrust and torque coefficients, were obtained from the CFD simulations and compared with the corresponding EFD data from the physical model tests. As shown in Figure 7, the CFD predictions demonstrated good agreement with experimental results generally. However, relatively larger discrepancies were observed at higher advance coefficients, specifically in the range of the advance ratios between 0.7 and 0.9, as presented in Table 5. In this range, the CFD model tends to under-predict thrust and over-predict torque, leading to increased deviations in the propeller efficiency (η_0). Nevertheless, the absolute magnitude of these errors remained small, being less than 0.009 in K_T and 0.0009 in K_Q.

Regarding the discrepancies observed in CFD predictions for a model-scale propeller, several researchers have noted that standard turbulence models, such as the k–ω SST model, exhibit limited accuracy at higher advance coefficients. Krasilnikov and Skjefstad (2023) ([22]) reported that the assumption of fully turbulent flow is not appropriate for model-scale CFD simulations and demonstrated noticeable discrepancies between model-scale and full-scale propeller performance. To address this issue, transition-sensitive models, such as the γ–Re_θ transition model, have been investigated for their ability to capture the laminar-to-turbulent transition on propeller blades in model-scale tests ([23], [24], [25], [26]). Therefore, better agreement could potentially be achieved by employing a transition model; however, this approach was beyond the scope of the present study.

In addition to the quantitative performance characteristics, the vortical structures in the propeller wake were visualized using the Q-criterion. Furthermore, the pressure distributions on the pressure and suction sides of the propeller blades at an advance ratio of $J = 0.9$ are presented in Figure 8 and Figure 9, respectively.

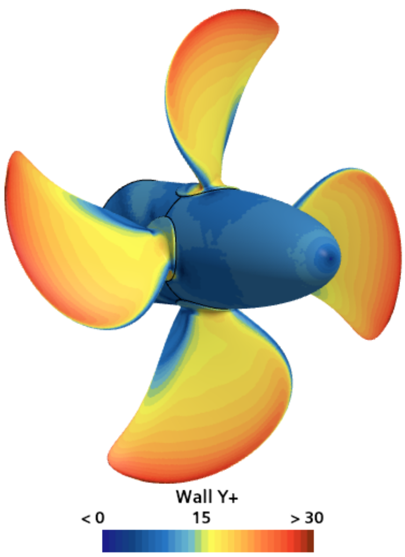

Figure 6: Wall y+ value of the model propeller.

Table 5: Comparison of propeller performance coefficients between the experiment results and the CFD prediction.

J	EFD		CFD		Error	
	K_T	K_Q	K_T	K_Q	K_T	K_Q
0.1	0.430	0.0586	0.420	0.0589	-2.30%	0.50%
0.2	0.390	0.0537	0.384	0.0545	-1.50%	1.50%
0.3	0.345	0.0484	0.343	0.0497	-0.60%	2.70%
0.4	0.298	0.0430	0.298	0.0444	0.00%	3.30%
0.5	0.253	0.0378	0.251	0.0392	-0.80%	3.70%
0.6	0.209	0.0326	0.203	0.0337	-2.90%	3.40%
0.7	0.166	0.0272	0.156	0.0281	-6.00%	3.30%
0.8	0.117	0.0214	0.108	0.0222	-7.70%	3.70%
0.9	0.062	0.0144	0.056	0.0153	-9.70%	6.30%
1.0	0.002	0.0064	-0.004	0.0074	N/A	N/A

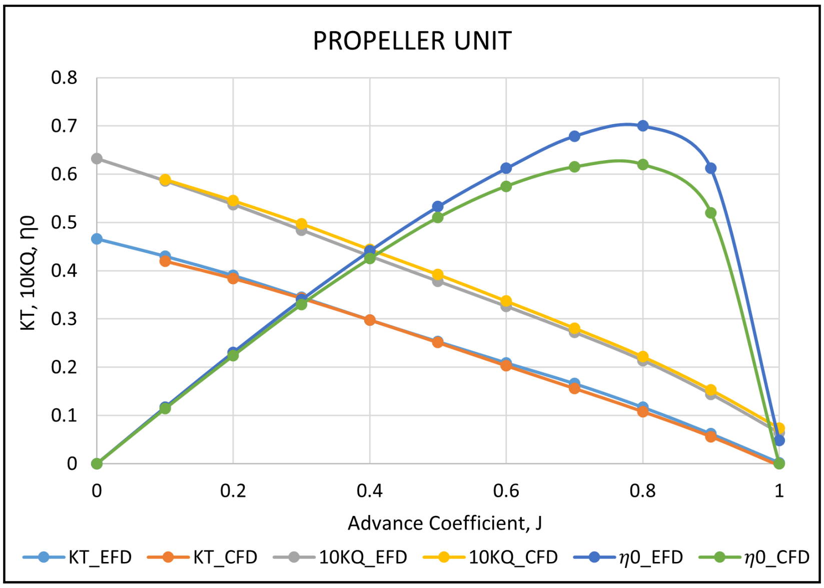

Figure 7: Propeller open-water performance curves: Comparison of propeller performance characteristics between the experimental results and the CFD predictions.

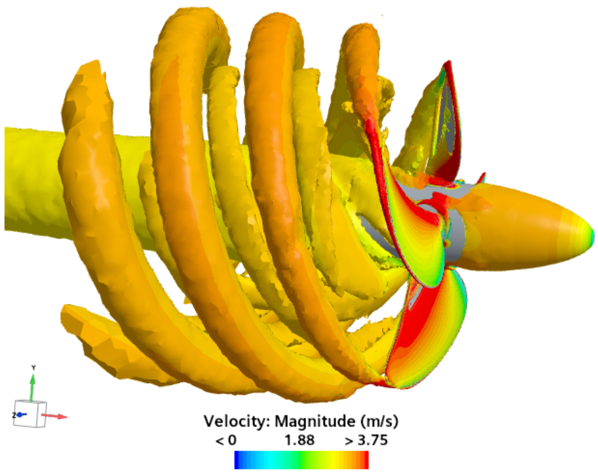

Figure 8: Velocity distribution Q-Criterion of the model propeller.

4.2 Ship Resistance Analysis

The calm-water resistance simulations were performed at full scale using the SOBC-1 hull geometry. To reduce computational cost, a half-body model was adopted. The simulations were conducted for vessel speeds ranging from 8 to 17 knots at the design waterline draft under even-keel conditions, with both the forward and aft drafts set to 11.0 m. The hull geometry included an appended rudder. Consistent with the wall-function approach, the average wall y^+ value on the vessel hull was maintained at approximately 300, as shown in Figure 10.

Hull roughness was also taken into account in the analysis. Even small surface imperfections can cause significant disturbances in the velocity field and alter the flow behavior, thereby affecting the hydrodynamic performance of the hull. In most cases, the roughness elements are too small to be directly resolved by the computational mesh. Therefore, a wall roughness model was employed by shifting the logarithmic layer of the inner boundary layer closer to the wall. The default hull roughness was set to 150 μm. This average hull roughness (R_{t50}) was converted into an equivalent sand-grain roughness height (k_s) for CFD simulations, following the approach suggested by Schultz (2007) ([27]).

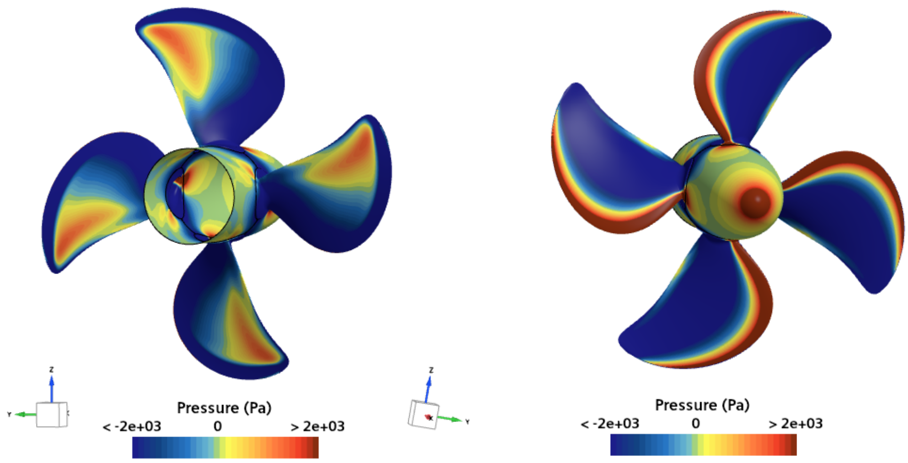

Figure 9: Pressure distribution on the propeller blades at the pressure side (left) and the suction side (right).

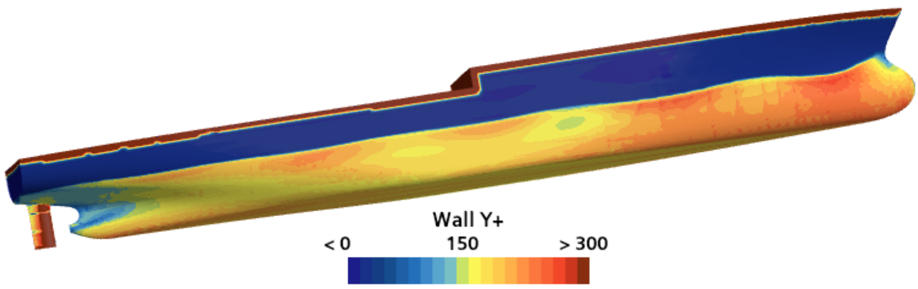

Figure 10: Wall y+ distribution on the hull surface.

Table 6 compares the physical model test results with the CFD predictions in terms of resistance, sinkage at the forward and aft perpendiculars, and trim angles at five representative speeds. A reasonable agreement between the EFD and CFD results is observed across the entire speed range. The CFD predictions of resistance show better agreement at higher speeds than at lower speeds, indicating that finer mesh resolution around the hull and free surface may be required at speeds below 12 knots to accurately capture the wave-making resistance associated with small-amplitude waves, since the present simulations employed the same mesh configuration for all speeds. The percentage error in resistance was found to vary between approximately 1.5% and 10% across the analyzed speed range. Good agreement was also obtained for the trim angles and sinkage at the forward perpendicular. However, the magnitude of sinkage at the aft perpendicular is relatively small and was not captured accurately with the current mesh resolution, suggesting that further near-hull mesh refinement may be required.

Figure 11 presents the flow field and free-surface elevation at a vessel speed of 15 knots. The results indicate that the Kelvin wake pattern is well captured by the CFD model.

4.3 Self-propulsion Point Prediction Analysis

Calm-water self-propulsion simulations were performed at ship scale using the full-scale SOBC-1 hull model, with the vessel free to heave and pitch and initially set at zero trim. The analyses were carried out at a single operating condition corresponding to a vessel speed of 15 knots at the DWL loading condition.

Full-body CFD simulations were conducted using two propulsion modeling approaches: (i) a fully rotating propeller and (ii) a body-force propeller method. For simulations with the actual propeller, a sliding-mesh (rigid-body motion) technique was applied to resolve the propeller rotation. For the body-force propeller approach, the propeller open-water performance curve (K_T–K_Q) from CFD prediction

Table 6: Comparison of EFD and CFD results for resistance, trim, and sinkage.

V_s	Resistance [kN]		Trim [deg]		Sinkage AP [m]		Sinkage FP [m]	
[knots]	EFD	CFD	EFD	CFD	EFD	CFD	EFD	CFD
8	126.24	140.10	-0.036	-0.044	-0.011	0.013	-0.131	-0.131
10	203.77	217.20	-0.063	-0.068	-0.006	0.017	-0.215	-0.209
12.5	345.79	357.20	-0.106	-0.110	0.004	0.030	-0.347	-0.334
15	557.69	567.81	-0.167	-0.168	0.025	0.047	-0.529	-0.511
17	871.96	885.20	-0.228	-0.228	0.049	0.072	-0.709	-0.700

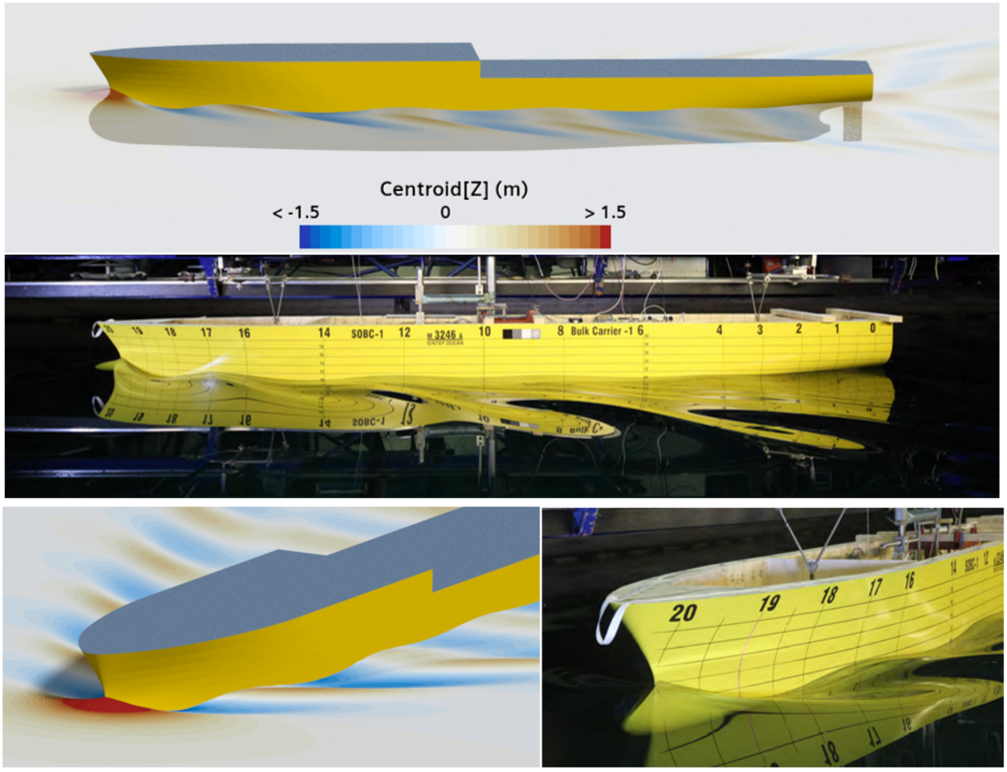

Figure 11: Wave Profile at 15 knots vessel speed.

was used to represent the thrust and moment characteristics of the virtual disk.

A refined mesh with a base cell size of 1.75 m was adopted for all SPP analyses with an actual rotating propeller. The geometry employed for the SPP simulations with the actual propeller is shown in Figure 1, while the corresponding computational domain and mesh distribution are presented in Figure 4. All simulations were performed using water properties corresponding to a temperature of 15°C, in accordance with the SINTEF Ocean reference report ([14]). The self-propulsion point was determined using a Proportional–Integral (PI) controller ([28]), which iteratively adjusted the propeller rotational speed to achieve equilibrium between the propeller thrust and the total ship resistance.

Figure 12 presents the free-surface wave profile and flow field for the self-propulsion case with an actual rotating propeller, where the propeller-induced vorticity and wake structures are well resolved. Conversely, when the body-force propeller method is applied, the detailed vortex shedding phenomena are not reproduced, as illustrated in Figure 12. Body-force propeller method cannot capture the unsteady flow characteristics.

Table 7 presents a comparison between the physical model test data (EFD) and the CFD results obtained from the self-propulsion analysis. In general, both self-propulsion simulation methods show good

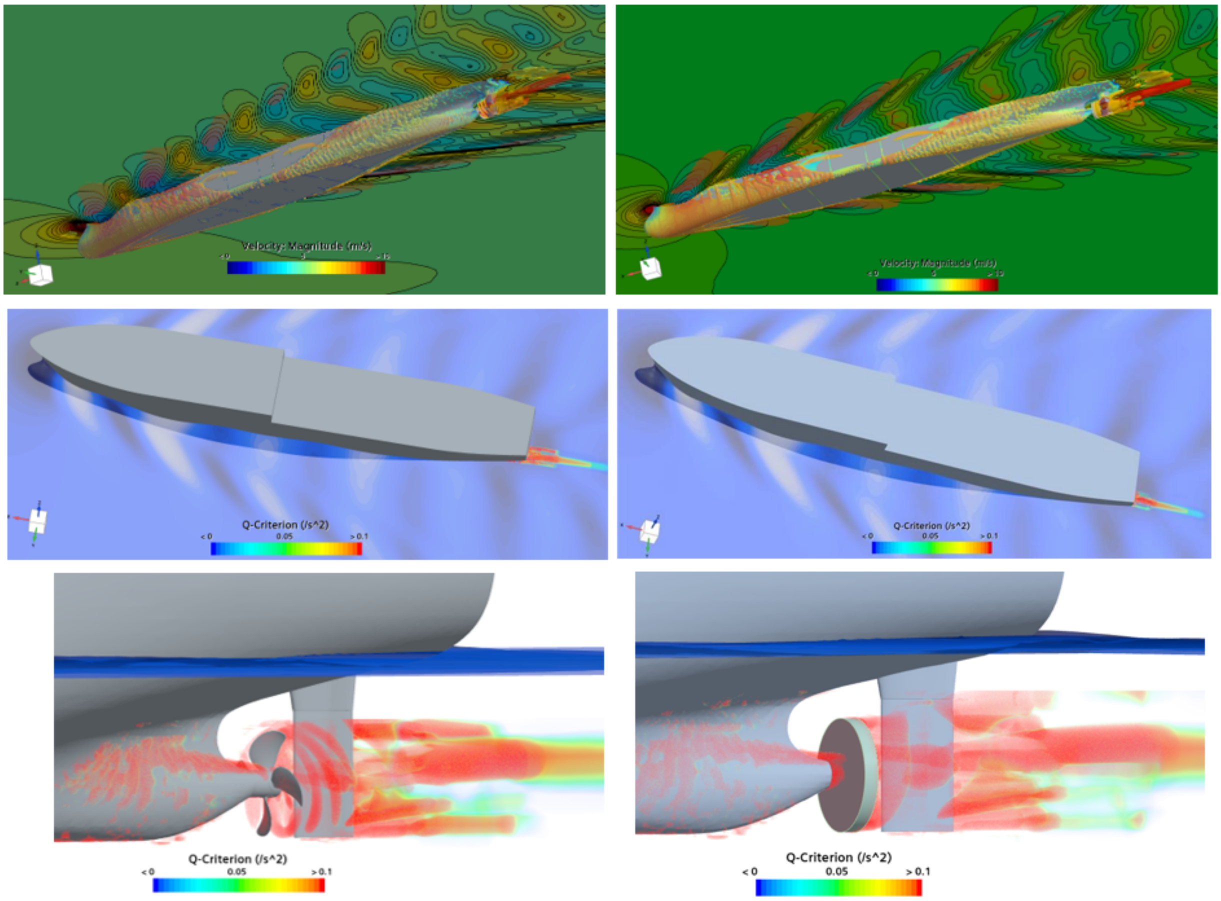

Figure 12: Comparison of flow patterns obtained from the SPP analysis using the rotating propeller (left) and the virtual disk model (right).

agreement with the traditional model test-based approach. The propeller rotational speed exhibited a difference of approximately 4%, while the estimated power differed by about 7%. The differences in dynamic trim and sinkage were very small in magnitude and can therefore be considered negligible. The brake power (P_B) was calculated from the propeller torque (Q) and the rotational speed (N) using the following equation.

$$P_B = \frac{2\pi NQ}{\eta_m} \tag{10}$$

The mechanical efficiency (η_m) was set to 0.97, as specified in the model test report ([14]).

Table 7: Vessel propulsion performance- comparison between EFD and CFD results.

	EFD	CFD_Prop	CFD_VD	Error_Prop [%]	Error_VD [%]
Prop. Shaft Rotation, N [rpm]	77.8	80.7	78.0	3.7	0.3
Brake Power, P_B [kW]	5975.2	6382	6307	6.8	5.6
Trim [deg]	-0.174	-0.176	-0.164	1.1	5.8
Sinkage AP [m]	0.033	0.036	0.041	9.1	24.3
Sinkage FP [m]	-0.544	-0.520	-0.505	4.4	7.2

When comparing the two propeller modeling methods, the body-force propeller approach showed better agreement with the results based on the model test to predict the self-propulsion point. Typically, rotating propeller simulations can resolve the flow field in greater detail, whereas the body-force propeller method represents a simplified or smoothed propeller action based on K_T-K_Q characteristics. The current results alone are not sufficient to definitively determine which propeller modeling approach is more accurate. However, the body-force propeller method appears to be more consistent with conventional model testing practices, which decouple propeller–hull interactions into several contributing factors such as wake fraction and relative rotative efficiency, and extrapolate the required power based on open-water performance data.

The brake power predictions from the two propeller modeling methods indicate that the body-force propeller (BFP) approach provides slightly better agreement with the model test results. In contrast, the rotating propeller approach yields lower errors in the prediction of dynamic sinkage and trim. In general, rotating propeller simulations resolve the flow field in greater detail, whereas the BFP method represents a simplified or averaged propeller action based on the K_T-K_Q characteristics and is unable to capture the detailed vortex structures generated by the propeller.

When considering the computational effort required for self-propulsion point analysis, the rotating propeller approach demands significantly higher computational resources due to the need for a much finer mesh and a smaller time step. Given the balance between accuracy and computational efficiency, the body-force method is considered a more practical choice for powering estimation. Nevertheless, it should be noted that the body-force propeller method cannot capture unsteady flow structures or complex flow interactions in the presence of energy-saving devices. Therefore, when detailed prediction of unsteady propeller flow characteristics is not required, the body-force propeller method is recommended.

4.4 Wake Study

A three-dimensional wake study was conducted at the propeller plane for the design waterline condition at a ship speed of 15 knots. The analysis was performed at model scale to enable a direct comparison with the physical model test data. A smooth hull condition was assumed in the simulations. An additional mesh refinement region was introduced around the stern and propeller plane to accurately capture the wake profile and resolve the flow field in the wake region.

The nominal wake fraction, axial (Taylor) wake fraction (ω_{ax}), tangential wake fraction (ω_T), and radial wake fraction (ω_R) were evaluated at the propeller plane. The distributions of ω_{ax}, ω_T, and ω_R are presented as functions of radial position and angular location. An angular position of 0° corresponds to the top vertical position, while 90° corresponds to the starboard side, consistent with the convention adopted in the SINTEF Ocean AS report ([14]).

The measurement plane is perpendicular to the propeller shaft and intersects the generator line of the propeller blade at $0.7R$, where R is the propeller radius. The tangential and radial wake fractions were obtained by normalizing the tangential and radial velocity components by the ship speed. The axial wake fraction was calculated using the following expression:

$$\omega_{ax} = 1 - \frac{V_A}{V} \tag{11}$$

Where, V_A is the axial velocity (speed of advance) and V is the ship speed in model scale.

A comparison was made between the CFD-predicted three-dimensional wake fields and the experimental data at sections located $0.398R$, $0.503R$, $0.702R$, $0.901R$, and $1.1R$ from the propeller center on the wake measurement plane. The comparison for three representative sections is presented in Figure 13. Overall, good agreement was observed for all three wake fractions. A small discrepancy in magnitude was noted for the tangential wake fraction at the $0.398R$ section, where the CFD predictions underpredicted the tangential velocity component. This discrepancy may be attributed to limitations of the RANS turbulence model in accurately capturing the complex rotational flow structures in the propeller inflow region. Overall, the CFD model was able to reproduce the measured wake field with satisfactory accuracy.

The 3D wake measurements showed acceptable velocity distributions and gradients that are typical of this vessel type and propulsion arrangement, with a peak axial wake fraction of approximately 0.60 near the propeller tip region, which closely agrees with the measurement data.

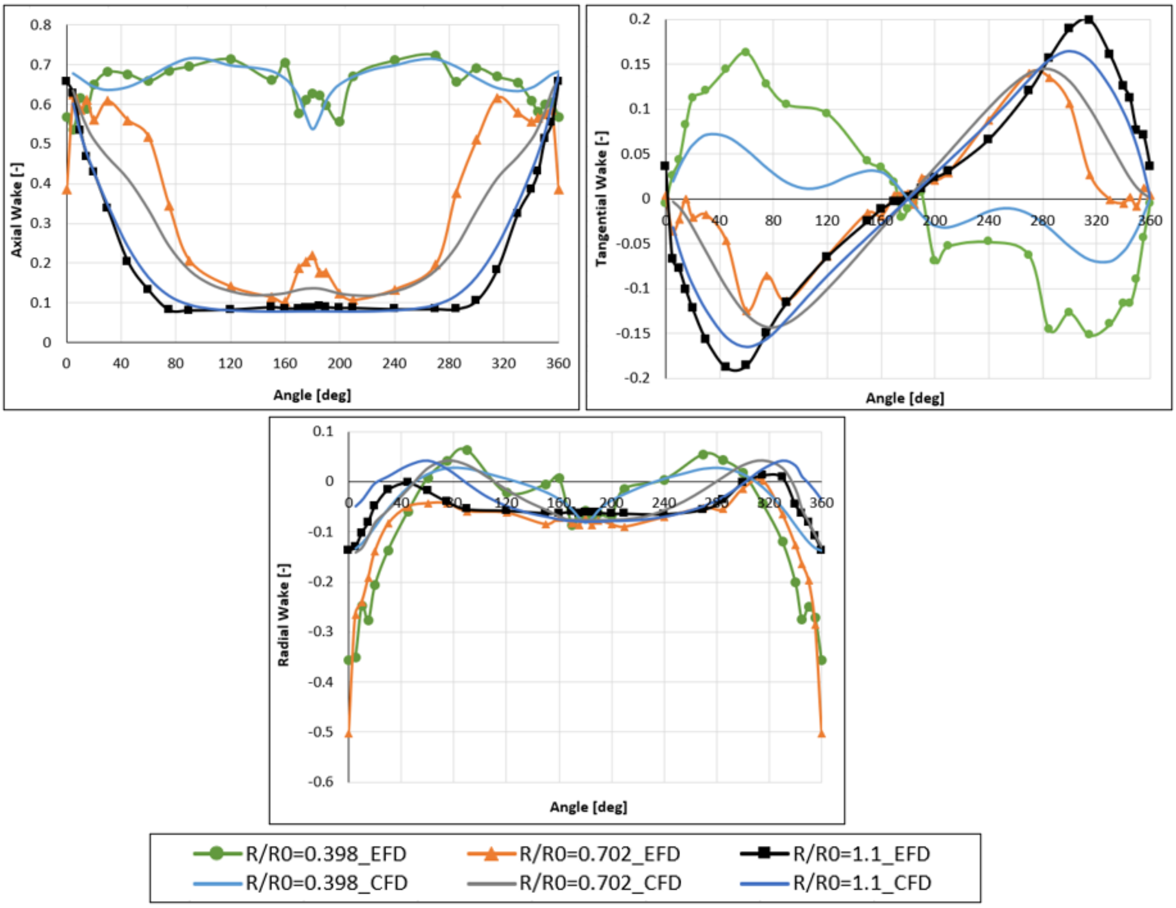

Figure 13: Comparison of Normalized axial, tangential, and radial velocity distributions at the propeller plane from EFD and CED analyses.

The normalized axial (Taylor) wake, together with the radial and tangential velocity components, was qualitatively assessed at the wake measurement plane. The RANS-predicted CFD solutions show good overall qualitative agreement with the model test data.

However, the numerical model fails to capture the highly complex and nonlinear wake structures localized around the propeller hub, as clearly illustrated in Figure 14. Significant discrepancies are observed in the regions around ±30°. While these differences may be partially attributed to the choice of turbulence model, higher-fidelity approaches such as LES or DES may provide more accurate predictions than RANS. The discrepancies could also result from inherent flow unsteadiness. Owing to the rounded hull geometry in the vicinity of the propeller shaft, vortex stretching and shedding are often highly unsteady, making accurate prediction of the local wake field particularly challenging.

Overall, the wake field was assessed as satisfactory and shows a reasonable agreement with the physical model test data.

5. Conclusion and Future Work

This study presented a step-by-step Computational Fluid Dynamics (CFD) investigation of the calm-water hydrodynamic performance of the SOBC-1 (SINTEF Ocean Bulk Carrier No. 1). The numerical framework covered propeller open-water performance, ship resistance, self-propulsion analysis, and wake

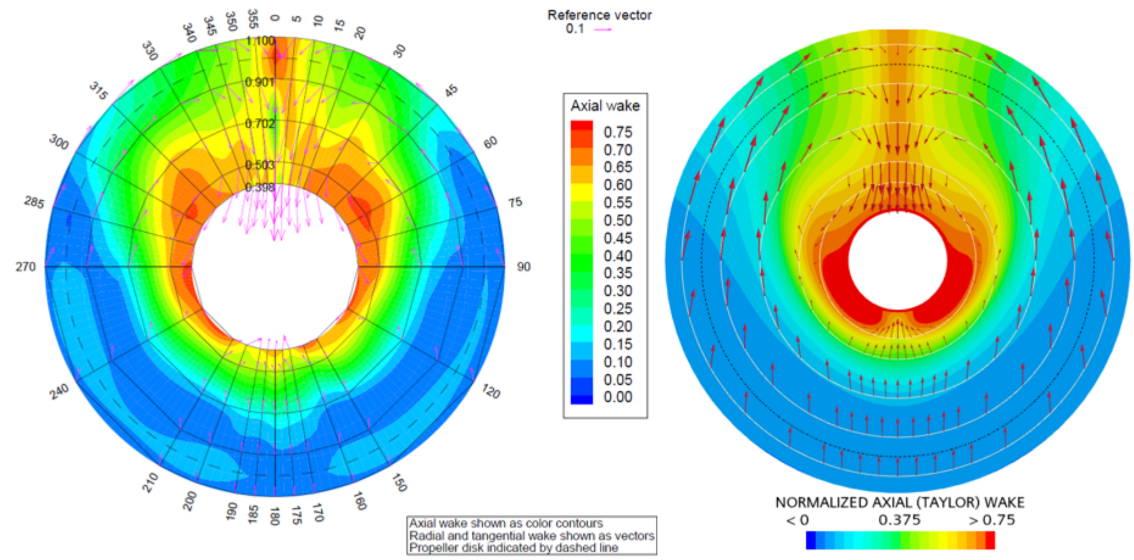

Figure 14: Comparison of normalized axial wake and normalized tangential, and radial velocity vector distributions at the propeller plane from EFD (left) and CFD (right) Analyses.

survey.

The predicted propeller open-water characteristics showed good agreement with the available physical model test data, demonstrating the capability of the adopted CFD methodology to accurately capture propeller thrust and torque behavior. The current CFD model under-predicts the thrust coefficient and over-predicts the torque coefficient at higher advance coefficients (J = 0.7-0.9). It is evident from the literature that transition models perform better than fully turbulent models. Therefore, a validation study employing the Gamma-ReTheta (γ-Re_θ) transition model should be conducted in future work.

Calm-water resistance simulations were performed at the design waterline using the appended hull form with free sinkage and trim conditions. The CFD-predicted resistance, sinkage, and trim results compared favorably with experimental measurements over the investigated speed range, confirming the robustness of the numerical setup and grid resolution strategy.

Self-propulsion simulations were conducted at the speed of 15 knots using two different propulsion modeling approaches: an actually rotating propeller employing a sliding-mesh technique and a body-force propeller representation using a virtual disk. Both approaches were able to predict the self-propulsion point (SPP) with satisfactory accuracy compared with physical model test data. The rotating propeller method provided improved resolution of unsteady propeller-induced flow structures, wake evolution, and vorticity, albeit at a significantly higher computational cost due to finer mesh and smaller time-step requirements.

Based on the findings of the present study, the body-force propeller method is recommended for routine powering estimation where global propulsion parameters are of primary interest, owing to its substantially reduced computational cost. Conversely, the actual rotating propeller approach should be considered for applications requiring detailed investigation of unsteady propeller-induced flow phenomena, wake structures, and propeller-hull interaction effects. Consistent with ITTC best-practice guidelines, the selection of the propulsion modeling approach should therefore be guided by the intended level of physical fidelity and the specific objectives of the numerical study.

The three-dimensional wake field validation demonstrates that the computational fluid dynamics (CFD) model reproduces the nominal wake field on the measurement plane with satisfactory reliability. The numerical framework accurately captures the characteristic velocity distributions, localized gradients, and a peak axial wake fraction of approximately 0.60 near the propeller tip, matching the physical experimental fluid dynamics (EFD) trends for this propulsion arrangement. Minor quantitative underpredictions in the tangential wake component at the inner radius ($0.398R$) and localized structural discrepancies near the propeller hub underscore the inherent limitations of the RANS turbulence modeling approach in highly rotational, separated flow regimes. Nevertheless, the global agreement across all axial, radial, and tangential wake fractions is thoroughly satisfactory, confirming that the validated numerical velocity fields provide a dependable hydrodynamic baseline for subsequent propeller-hull interaction and self-propulsion point analyses for this vessel type.

Acknowledgements

The authors gratefully acknowledge the support of the National Research Council's Ocean, Coastal and River Engineering Research Centre in the execution of this research. The authors also sincerely thank SINTEF Ocean for providing the physical model test data and the geometrical models of the SOBC-1 vessel and the propeller, which were essential for the development, verification, and validation of the CFD simulations presented in this study.

References

[1] V. Krasilnikov, V. S. Skjefstad, K. Koushan, and H. J. Rambech. A calibration study with cfd methodology for self-propulsion simulations at ship scale. *Journal of Marine Science and Engineering*, 11(7):1342, 2023. https://doi.org/10.3390/jmse11071342.

[2] M. F. Islam and F. Jahra. Methodologies to Predict Hydrodynamic Characteristics of Pusher and Puller Podded Propulsors in Oblique Flows. *Transactions of the Royal Institution of Naval Architects Part A: International Journal of Maritime Engineering*, 158:299–314, 2016.

[3] D. C. Seo, F. Jahra, and J. Wang. Cfd simulation of hydrodynamic interaction between a ship and a podded propeller using a body force method. Proceedings of the 43rd international conference on ocean, offshore and arctic engineering (omae 2024), singapore expo, singapore, june 9-14, 2024.

[4] A. Yu, D. Wang, and G. Chen. Verification and Validation for the Resistance of a KRISO Container Ship in Calm Water. ISOPE Conference, International Society of Offshore and Polar Engineers, pp. 4479–4485, ISBN: 978-1-880653-85-2, ISSN: 1098-6189, 2019.

[5] H. Wang, X. Gong, Z. Yu, and X. Xianbo. Numerical Study on Hydrodynamic Performance of Ducted Propeller Based on Improved Body Force Model. *Chinese Journal of Ship Research*, 18(4), 2023. DOI: 10.19693/j.issn.1673-3185.02920.

[6] R. V. Wilson, P. M. Carrica, and F. Stern. URANS Simulations for a High-Speed Transom Stern Ship with Breaking Waves. *International Journal of Computational Fluid Dynamics*, 20(2):105–125, 2006.

[7] F. Jahra, M. Islam, W. Thanyamanta, and D. Molyneux. Investigation of hydrodynamic loads and flow patterns near an escort tug in oblique flows. International conference on ocean, offshore and arctic engineering (omae2015), st. john's, canada, may 31-june 5, 2015.

[8] M. Islam, F. Jahra, R. Rayn, D. Molyneux, and H. Lee. Hydrodynamic Performance of a FPSO in Highly Oblique Flow Conditions. OMAE 2015, International Conference on Ocean, Offshore and Arctic Engineering, St. John's, Canada, May 31-June 5, 2015.

[9] Y. M. Ahmed, O. B. Yaakob, M. F. A. Rashid, and A. H. Elbatran. Determining Ship Resistance Using Computational Fluid Dynamics (CFD). *Journal of Transport System Engineering*, 2(1):20–25, 2015.

[10] S. Aram and P. Mucha. Computational Fluid Dynamics Analysis of Different Propeller Models for a Ship Maneuvering in Calm Water. *Ocean Engineering*, 276:114226, 2023. DOI: 10.1016/j.oceaneng.2023.114226.

[11] G. Deng, P. Queutey, E. Guilmineau, A. Leroyer, M. Visonneau, and J. Wackers. Ship Maneuvering Simulation with CFD Approach. 25ème Congrès Français de Mécanique, Nantes, France, hal-03685470v2, 2022.

[12] L. Zou, L. Larsson, and M. Orych. Verification and Validation of CFD Predictions for a Manoeuvring Tanker. *Journal of Hydrodynamics*, 22(5):438–445, 2010.

[13] JORES Committee. JORES Website. [https://jores.net/], 2023.

[14] H. J. Rambech. Report: Calm Water Performance Tests, SOBC-1 (SINTEF Ocean Bulk Carrier No.1). SINTEF Report, Project No. 302006033-09, August 25, Enterprise Number: NO 937 357 370 MVA, 2021.

[15] SINTEF. SOBC-1 Benchmark Data Website. [https://github.com/SINTEF/sobc-1-benchmark-data], 2023.

[16] V. Krasilnikov. SINTEF Ocean Benchmark Bulk Carrier "SOBC-1". Presentation, SINTEF Ocean, Department of Ships and Ocean Structures, Marine CFD, International Collaboration Network in Marine Technology, 03.05.2022, 2022.

[17] F. R. Menter. Two-equation eddy-viscosity turbulence modeling for engineering applications. *AIAA Journal*, 32(8):1598–1605, 1994.

[18] International Towing Tank Conference. Uncertainty analysis in CFD verification and validation methodology and procedure. Revision 05 7.5-03-01-01, ITTC, 2024.

[19] P. J. Roache. *Verification and Validation in Computational Science and Engineering*. Hermosa Publishers, Albuquerque, New Mexico, 1998.

[20] F. Stern, R. Wilson, and J. Shao. Quantitative v&v of cfd simulations and certification of cfd codes. *International Journal for Numerical Methods in Fluids*, 50:1335–1355, 2006.

[21] T. Xing and F. Stern. Factors of safety for Richardson extrapolation. *Journal of Fluids Engineering*, 132(6):061403, 06 2010. https://doi.org/10.1115/1.4001771.

[22] V. Krasilnikov and V. Skjefstad. Sobc-1 an open science validation dataset for conventional and wind-assisted ship propulsion. 25th numerical towing tank symposium (nutts), Ericeira, Portugal, 2023.

[23] K. W. Kim, K. J. Paik, J. H. Lee, S. S. Song, M. Atlar, and Y. K. Demirel. A study on the efficient numerical analysis for the prediction of full-scale propeller performance using cfd. *Ocean Engineering*, 240:109931, 2021. https://doi.org/10.1016/j.oceaneng.2021.109931.

[24] M. Bennaya, J. Gong, M. M. Hegaze, and W. Zhang. Numerical simulation of marine propeller hydrodynamic performance in uniform inflow with different turbulence models. *Applied Mechanics and Materials*, 389:1019–1025, 2013. DOI:10.4028/www.scientific.net/AMM.389.1019.

[25] A. Moran-Guerrero, L. M. Gonzalez-Gutierrez, A. Oliva-Remola, and H. R. Diaz-Ojeda. On the influence of transition modeling and crossflow effects on open water propeller simulations. *Ocean Engineering*, 156:101–119, 2018. DOI:10.1016/j.oceaneng.2018.02.068.

[26] J. Baltazar, D. Rijpkema, and J. F. Campos. On the use of the $\tilde{Re}_\theta$ transition model for the prediction of the propeller performance at model-scale. *Ocean Engineering*, 170:6–19, 2018. https://doi.org/10.1016/j.oceaneng.2018.10.005.

[27] M. P. Schultz. Effects of coating roughness and biofouling on ship resistance and powering. *Biofouling*, 23(5):331–341, 2007. DOI:10.1080/08927010701461974.

[28] M. Nuutinen. Automated self-propulsion point search algorithm for ship performance cfd simulations. Proceedings of the sixth international symposium on marine propulsors (smp'19), Rome, Italy, 2019.